# Journal of Materials Chemistry A

Accepted Manuscript






ROYAL SOCIETY OF CHEMISTRY

www.rsc.org/materialsA

Journal Name

ARTICLE

# Formation of $Fe_3O_4$@$MnO_2$ ball-in-ball hollow spheres as a high performance catalyst for enhanced catalytic performances

Received 00th January 20xx,
Accepted 00th January 20xx

DOI: 10.1039/x0xx00000x

www.rsc.org/

Shouwei Zhang[a], Qiaohui Fan[b], Huihui Gao[a], Yongshun Huang[c], Xia Liu[c], Jiaxing Li*[c,d], Xijin Xu*[a], Xiangke Wang*[d]

While the synthesis of heterogeneous catalysts is well established, it is extremely challenging to fabricate complex hollow structures with mixed transition metal oxides. Herein, we report a facile *in situ* growth process of $SiO_2$@$Fe_3O_4$@$MnO_2$, followed by etching method to synthesize a hierarchical hollow structure, namely $Fe_3O_4$@$MnO_2$ ball-in-ball hollow spheres ($Fe_3O_4$@$MnO_2$ BBHs). The as-prepared $Fe_3O_4$@$MnO_2$ BBHs were applied to degrade methylene blue (MB) by catalytic generation of active radical from peroxymonosulfate (PMS), exhibiting the merits of excellent catalytic performance, easy separation, good stability and recyclability. In this architecture, the degradation process can be divided into three layers. The outer hierarchical $MnO_2$ nanosheets could accumulate and transport the pollutants by electrostatic interactions and catalyze the generation of active radical for degradation. Both inner $MnO_2$ nanosheets and outer $Fe_3O_4$ hollows could produce active radicals to accelerate the pollutant degradation. The active catalytic sites also existed in inner $Fe_3O_4$ hollows, which could further degrade the high concentrated pollutants in hollows. This work provided new strategies for the controllable synthesis of complex hollow structures and their application in environmental remediation.

## 1 Introduction

Over the last decades, industrial activities generate large amounts of organic hazardous substances discharged into the environment. The organic wastes can be found in many industries as by-products such as petroleum refining, petrochemical, pharmaceutical, plastic, pesticides, chemical industries, agrochemicals, and pulp and paper industries. The organic pollutants e.g. dyes and phenolic compounds, are highly toxic to natural degradation and have caused serious issues to the ecosystem even at low concentrations.[1, 2]

Recently, many treatment approaches have been investigated for the environmental removal of organic pollutants in aqueous phase, including advanced oxidation processes (AOPs), direct photolysis, adsorption and etc, have been developed to remove organic compounds from wastewater.[3-7]

Among them, AOPs have been commonly suggested as the cost-effective mechanisms for the removal of persistent organic pollutants from aqueous systems.[8-12] As one of the most intensively investigated AOPs, hydroxyl radical (·OH) generated from $H_2O_2$ through Fenton reaction is a highly reactive and strong oxidizing radical to degrade organic compounds.[13, 14] However, the demanding pH of acid environment and instability of $H_2O_2$ under ambient temperature limited its application.[15, 16] To overcome these disadvantages, sulfate radical ($SO_4^{\cdot-}$), which can be generated from persulfate (PS) and peroxymonosulfate (PMS), attracted increasing interests as an alternative to ·OH for the degradation of recalcitrant organic pollutants.[16] Activated PMS oxidation has been regarded as an interesting treatment method in two aspects. First, PMS is easier to be activated compared with $H_2O_2$.[17] Second, the activation of PS system requires acid environment and high oxygen in solution. Moreover, PMS is mainly activated by heating, UV irradiation and transition metal.[18, 19] However, the former are restricted in practical application owing to their high energy input, thus more and more studies related to the PMS activation have focused on transition metals.[20-22] Among the various transition metal catalysts, cobalt stands out as one of the most efficient elements.[23, 24] However, leaching of potentially carcinogenic $Co^{2+}$ is still inevitable in $Co^{2+}$/PMS systems, thus resulting in secondary metal pollution.[16, 20, 25] Therefore, increasing attention has been paid to the development of novel hybrid materials with incorporated other metal active sites for new catalytic system.[15, 21, 26, 27]

Manganese-based materials have also been widely applied in AOPs due to its unique $Mn^{2+}$/$Mn^{4+}$ redox loop and lower toxicity to the environment as compared with $Co^{2+}$.[15, 28, 29] Therefore, manganese-based materials have been reported as

[a] School of Physics and Technology, University of Jinan, Shandong, 250022, P. R. China. E-mail: sps xuxj@ujn.edu.cn
[b] Key Laboratory of Petroleum Resources, Gansu Province/Key Laboratory of Petroleum Resources Research, Institute of Geology and Geophysics, Chinese Academy of Sciences, Lanzhou 730000, P.R. China
[c] Key Laboratory of Novel Thin Film Solar Cells, Institute of Plasma Physics, Chinese Academy of Sciences P.O. Box 1126, 230031 Hefei, P. R. China TEL:+86-551-65596617, FAX: +86-551-65591310, E-mail: lijx@ipp.ac.cn (J. Li)
[d] NAAM Research Group, Faculty of Science, King Abdulaziz University, Jeddah 21589, Saudi Arabia. E-mail: xkwang@ipp.ac.cn

Electronic Supplementary Information (ESI) available: [Experimental sections and the pseudo first-order rate constant of the degradation of MB under different conditions]. See DOI: 10.1039/x0xx00000x

most promising alternatives to $Co^{2+}$ systems for PMS activation.[15, 28, 29] However, manganese-based materials tend to form superfine particles in solution, making it difficult for solid-liquid separation.[4, 29] In contrary, magnetic $Fe_3O_4$-based materials not only have unique and novel properties but also could be easily separated from solution by external magnetic field. Moreover, $SO_4^{\cdot-}$ can be generated effectively when PMS is combined with $Fe^{2+}$.[18, 27] However, most iron oxide-based catalysts in AOPs have tended to agglomerate during operation, resulting in a significant deterioration of the catalytic activity. Another issue of concern is that the catalysts are unstable and the catalytic sites are contaminated readily when directly exposed in bulk reaction solution. Accordingly, it was considered that transferring the AOPs into a nanoreactor might be an ideal way to address the above difficulties. In addition, catalysts confined in the inner space of nanoreactors maybe display enhanced catalytic performance.

Besides the control in composition, the realization of high efficiency catalytic reactions also depends on the rational design of catalyst structures.[8, 28, 30] It should be noted that catalysts with similar compositions but different morphologies demonstrate substantially distinct catalytic activities.[31-33] One of the effective strategies is the employment of hollow structures with different complex interiors as advanced electrodes, such as core-shell, yolk-shell, and multishell structures, because these special structures could inherit the advantages from both nanosized building blocks and hollow structures. Among all kinds of well-defined architectures, the catalysts with hierarchical and hollow nanostructures, especially multi-shell hollow spheres, have received more interest due to their special properties, including large surface area, accessible active site, and confined interior space, which promote the efficiency of loading and increase the contact surface between the components and the pollutants.[34-36] In comparison to single shell hollow spheres, the multi-shell ones possess more shells and isolated chambers. These constituent subunits often divide the hollow interiors into several regions with the formation of microenvironments to confine the pollutants, leading to higher reactant concentrations in the interior sections of the catalysts, which generate driving forces to enhanced catalytic activities.[37, 38] Hollow structures with multi-shells have unique structural attributes that make them excellent candidates for high performance catalysts: (1) their nanocrystal subunits provide high specific surface areas with numerous active sites for AOPs, [39, 40] (2) nanoscale building blocks can also shorten the path of reactant and enhanced catalytic rate,[41] (3) thin hollow structures readily expand in three-dimensions to buffer the mechanical stresses.[34, 36]

Therefore, equipping manganese-iron hybrid materials with hierarchical hollow architectures may not only expose more active surface sites and generate more separate nanoreactors to prevent self-aggregation, but also provide extra microenvironments and free voids as buffer zones to avoid structural collapse, as well the easy separation by magnet, resulting in the construction of superior catalysts for AOPs. However, to the best of our knowledge, studies on the possibility of integrating novel multi-shell hollow $Fe_3O_4$ and hierarchical $MnO_2$ nanosheets with hollow structure for AOPs are still in a premature stage.

Inspired by this proposal, we report a facile method to synthesize a novel ball-in-ball hollow structure of $Fe_3O_4$@$MnO_2$. The catalytic activity of $Fe_3O_4$@$MnO_2$ ball-in-ball hollow spheres ($Fe_3O_4$@$MnO_2$ BBHs) as a catalyst was tested for the degradation of methylene blue (MB) with the assistance of PMS oxidant. Moreover, a plausible mechanism is proposed to explain the enhanced catalytic performance. This study may provide novel ball-in-ball hollow spheres with reasonable catalytic systems for the improvement of Fenton-like catalysis in environmental remediation.

## 2 Experimental sections

### 2.1 Synthesis of $SiO_2$ spheres

The $SiO_2$ spheres were prepared according to Stöber's method.[42] For a typical process, tetraethyl orthosilicate (TEOS, 6.0 mL) were rapidly added into a mixture of ethanol (120 mL), deionized water (10 mL), and concentrated ammonia solution (3.2 mL) under the vigorous stirring. The mixture was allowed to react for 24 h at room temperature. The resultant product was separated and collected by centrifugation, followed by washing with deionized water and ethanol.

### 2.2 One-pot preparation of $SiO_2$@$Fe_3O_4$/C spheres

The core-shell $SiO_2$@$Fe_3O_4$/C spheres were prepared by solvothermal approach.[42] Briefly, $SiO_2$ (400 mg) spheres and ferrocene (200 mg) were homogenously stirred and ultrasonicated in 65 mL acetone. Then, 2 mL $H_2O_2$ was slowly added and stirred for 30 min. After that, the mixture was transferred into 100 mL autoclave and then heat to 200 $^{o}$C for 24 h. After the reaction, the autoclave was cooled to room temperature naturally. The obtained products were washed with acetone and ethanol.

### 2.3 Preparation of $Fe_3O_4$@$MnO_2$ ball-in-ball hollow spheres

Hierarchical $MnO_2$ nanosheets were grown on $SiO_2$@$Fe_3O_4$/C spheres with the aid of the redox reaction between $KMnO_4$ and carbon by adding $SiO_2$@$Fe_3O_4$/C spheres (200 mg) into 0.01 M $KMnO_4$ solution (70 mL) under stirring. Subsequently, the mixture was transferred into 100 mL autoclave and kept at 160 $^{o}$C for 12 h. After cooling the autoclave to room temperature, the product was etched by 2 M NaOH solution to remove the $SiO_2$ core. The final products, the $Fe_3O_4$@$MnO_2$ ball-in-ball hollow spheres, were obtained after centrifugation and washed by deionized water.

As control catalysts, the hierarchical $MnO_2$ hollow/solid spheres and $Fe_3O_4$ hollow/solid spheres were also prepared, respectively. (See in Supporting Information, SI)

### 2.4 Characterization

Powder X-ray diffraction (XRD) data were collected using a D/MAX2500V diffractometer using Cu $K_\alpha$ radiation (λ = 1.5418 Å). The structural information of the samples were measured by a Fourier transform spectrophotometer (FT-IR, Avatar 370, Thermo Nicolet) using the standard KBr disk method. X-ray photoelectron spectroscopy (XPS) was performed using



 

ESCALAB250 with Mg $K_\alpha$ as the source and the C 1s peak at 284.6 eV as an internal standard. The Brunauer-Emmett-Teller (BET) surface area of the catalysts was determined by a multi-point BET method. The morphologies and compositions were characterized using a JEOL JSM-6330F scanning electron microscopy (SEM) instrument operated at a JEOL-2100 field emission transmission electron microscope (FETEM) at an accelerating voltage of 200 kV.

**2.5 Catalytic degradation procedure**

Methylene blue (MB) degradation was performed in a 250 mL conical flask with MB (30 mg/L) solution and dipped in a constant-temperature water bath (298 K). The catalysts (300 mg/L) was first added to the solution and stirred for 120 min and then PMS (20 mM) was added to the solution to start the degradation. Solution pH was adjusted by 0.01 M $H_2SO_4$ or NaOH. At defined time intervals, an aliquot of 3 mL solution was withdrawn by a syringe, which was immediately quenched by ethanol (3 mL). The catalysts were separated using magnet, and the concentration of MB (λ=664 nm) was determined using a UV-vis spectrometer. The effects of catalyst dosages, PMS and MB concentrations, reaction temperature were investigated. The effects of foreign ions ($Cl^-$, $NO_3^-$, $SO_4^{2-}$, $ClO_4^-$, $Na^+$, $K^+$, $Ca^{2+}$) at 0.1 M on the degradation reaction were studied. The experiments were carried out under the same reaction conditions with MB (30 mg/L), PMS (20 mM), pH~7.98 and the used catalysts (300 mg/L) at 298 K. Various model pollutants (victoria blue B (VB), rhodamine B (RhB), methyl orange (MO), phenol and methyl violet (MV)) at 30 mg/L on the degradation reaction were studied. The experiments were carried out under the same reaction conditions with PMS (20 mM), pH~7.98 and the used catalysts (300 mg/L) at 298 K. In addition, two sets of quenching tests were carried out to determine the radical species formed in the catalytic system by using *tert*-butyl alcohol (TBA) and ethanol as the radical scavengers.

## 3 Results and discussion

**3.1 Material characterization**

A schematic illustration of the synthetic route is depicted in Figure 1 for the fabrication of $Fe_3O_4$@$MnO_2$ ball-in-ball hollow spheres ($Fe_3O_4$@$MnO_2$ BBHs). Specifically, a facile solvothermal synthesis was used to produce $SiO_2$@$Fe_3O_4$/C solid spheres by using a simple and inexpensive $SiO_2$ (Stöber's method) template-directed coating method with ferrocene as iron and carbon sources, constructing a double-layer coating of the inner $Fe_3O_4$ layer and the outer C layer simultaneously on $SiO_2$ surface. The freshly obtained $SiO_2$@$Fe_3O_4$/C solid spheres were further treated with $KMnO_4$ under hydrothermal conditions by growing hierarchical $MnO_2$ nanosheets on $SiO_2$@$Fe_3O_4$/C spheres to form $SiO_2$@$Fe_3O_4$@$MnO_2$ spheres via redox reactions between $KMnO_4$ and carbon layer. The product exhibited yolk-shell structure due to the loss of carbon source in the redox reaction. The removal of $SiO_2$ cores was conducted by NaOH etching to generate the desired $Fe_3O_4$@$MnO_2$ BBHs.

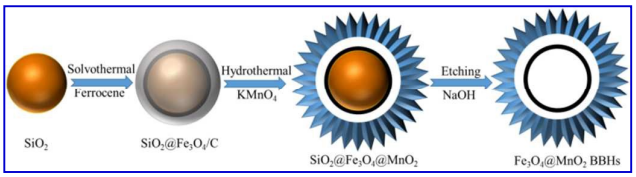


Figure 1. Schematic illustration for preparation of $Fe_3O_4$@$MnO_2$ BBHs.

To understand the evolution and crystalline structure of the $Fe_3O_4$@$MnO_2$ BBHs, the XRD patterns of $SiO_2$ and each composite are investigated (Figure 2A). For the $SiO_2$ spheres, a broad band between 20 and 30° is observed due to its amorphous structures.[43] After the solvothermal treatment with ferrocene, the diffraction pattern of $SiO_2$@$Fe_3O_4$/C can be well indexed to $Fe_3O_4$ (JCPDS 19-0629).[43] The average crystal sizes of the $Fe_3O_4$ nanoparticles estimate by using Scherrer's formula are ~7 nm, which are in good agreement with the TEM results. In addition, there are no obvious diffraction peaks corresponding to graphite carbon or other impurities in the XRD pattern, suggesting the thin and amorphous nature of the outer carbon shell. After the redox reaction under hydrothermal condition, the diffraction pattern of $SiO_2$@$Fe_3O_4$@$MnO_2$ can be well indexed to birnessite type $MnO_2$ (JCPDS No. 42-1317).[44, 45] For as-prepared $Fe_3O_4$@$MnO_2$ BBHs, the major diffraction peaks of $MnO_2$ and $Fe_3O_4$ are much clearer, indicating the removal of the $SiO_2$ core the etching process.

The FTIR spectra of the samples are presented in Figure 2B. For the $SiO_2$ spheres, the strong absorption peak at 3445 $cm^{-1}$ was assigned to the stretching vibration of O-H. The transmission spectrum showed bands at 1105, 802, and 472 $cm^{-1}$, which were presumably due to asymmetric stretching, symmetric stretching, and bending modes of Si-O-Si, respectively.[42] After treated with ferrocene to $SiO_2$@$Fe_3O_4$/C, the stretching vibrations of the Fe-O functional group were detected at 462 and 568 $cm^{-1}$.[30] Two new peaks at 1637 and 1407 $cm^{-1}$ were found and assigned as carboxylate groups, which were derived from the outer hydrothermal carbon layer.[30] As for $SiO_2$@$Fe_3O_4$/$MnO_2$, the bands at 447 and 514 $cm^{-1}$ could be attributed to Mn-O stretching vibrations in $MnO_2$, no peaks of carbon indicated the carbon was reacted via the redox reaction. Finally, the absence of $SiO_2$ signal (1105 $cm^{-1}$) suggested the removal of $SiO_2$ core by NaOH etching process.

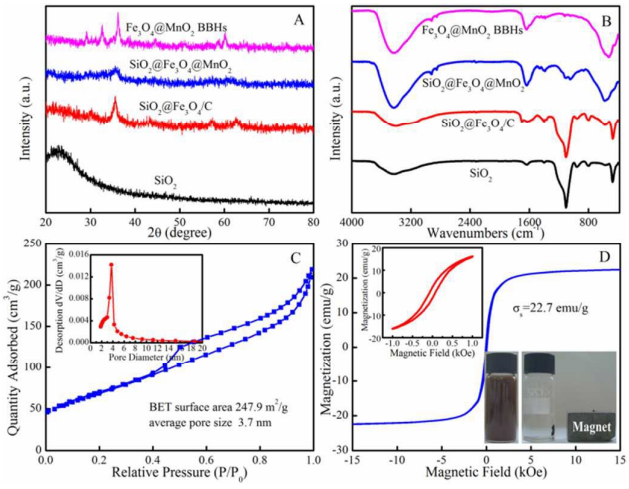


Figure 2. The XRD patterns (A) and FT-IR spectra (B) of the as-prepared catalysts, $N_2$ adsorption/desorption isotherm and pore size distribution (C) and magnetization curves (D) of $Fe_3O_4$@$MnO_2$ BBHs. The inset is a digital photograph of the magnetic separation.

The surface area and pore-size distribution are well-known to be important for catalytic performances. The BET surface area and average pore sizes of $Fe_3O_4$@$MnO_2$ BBHs were calculated to be ~247.9 $m^2$/g and ~3.7 nm, respectively (Figure 2C). The high surface area of the $Fe_3O_4$@$MnO_2$ BBHs will provide abundant active sites for PMS activation in the AOPs. The pore size distribution of ~2-7 nm will guarantee efficient transportation of pollutants to the catalysts, leading to enhanced catalytic properties.

The magnetization curve of the $Fe_3O_4$@$MnO_2$ BBHs is presented in Figure 2D. The saturation magnetization value was measured to be ~22.7 emu/g, the inset digital picture suggested the easy separation of the catalyst from the solution by a magnet.

The elemental valences of the $Fe_3O_4$@$MnO_2$ BBHs were studied by XPS (Figure 3). The survey spectrum clearly detected the existence of Fe, Mn and O elements (Figure 3A), while Figure 3B to F collected the high resolved XPS spectra of Fe 2p, Mn 2p, O 1s, Si 2p and C 1s, respectively. Two bands with binding energies of ~710.8 and ~724.1 eV were assigned to Fe $2p_{3/2}$ and Fe $2p_{1/2}$, respectively (Figure 3B). These bands were consisted of $Fe^{2+}$ from FeO and $Fe^{3+}$ from $Fe_2O_3$, which were typical characteristics of $Fe_3O_4$ structure.[46] The Mn $2p_{3/2}$ peak centered at ~641.9 eV and Mn $2p_{1/2}$ peak at ~653.5 eV with a spin-energy separation of ~11.6 eV were in good agreement with those reported for $MnO_2$ (Figure 3C).[45] The O 1s spectrum showed two peaks at ~529.6 and ~531.3 eV, which can be assigned to the lattice oxide oxygen and adsorbed oxygen or surface hydroxyl species (Figure 3D). The absence of peaks in the high resolved Si 2p and C 1s XPS spectra indicated the absence of Si and C elements (Figure 3E and F), indicating the complete removal of $SiO_2$ by NaOH, etching and the consumption of carbon by $KMnO_4$ during the redox reaction, respectively. The XPS results clearly proved the successful fabrication of $Fe_3O_4$@$MnO_2$ ball-in-ball hollow spheres.

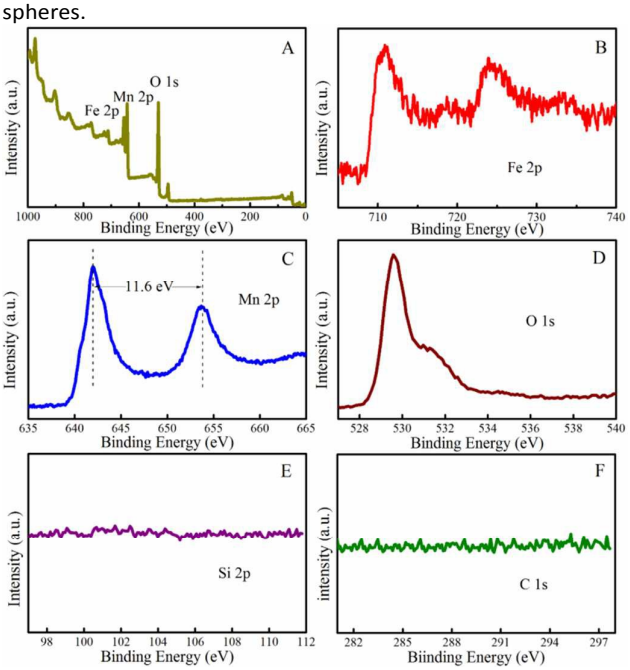


Figure 3. The XPS spectra of $Fe_3O_4$@$MnO_2$ BBHs: survey spectrum (A), high resolution Fe 2p (B), high resolution Mn 2p (C), high resolution O 1s (D), high resolution Si 2p (E) and high resolution C 1s (F).

The SEM and TEM images of the samples are also detected and shown in Figure 4. The as-prepared $SiO_2$ template had smooth surfaces and existed as monodisperse spheres with diameters about 300-400 nm (Figure 4A and B). The core-shell $SiO_2$@$Fe_3O_4$/C spheres obtained from solvothermal treatment preserved the smooth surfaces, but with uniform coating layers of ~50-60 nm as deep-contrast inner $Fe_3O_4$ layer and light-contrast outer carbon layer, respectively (Figure 4C and D). For $SiO_2$@$Fe_3O_4$@$MnO_2$ (Figure 4E and F), an obvious void was observed between the $Fe_3O_4$ and the external shell, which was due to loss of the carbon source in the redox reaction with $KMnO_4$ solution. Meanwhile, rough surfaces were detected as hierarchical nanosheets generated from the redox reaction.

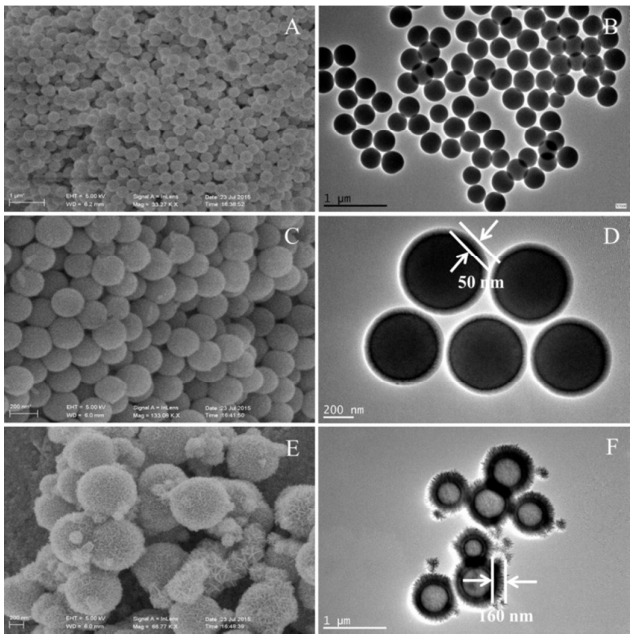


Figure 4. The SEM and TEM images of $SiO_2$ template (A and B), $SiO_2$@$Fe_3O_4$/C (C and D) and $SiO_2$@$Fe_3O_4$@$MnO_2$ (E and F).

The SEM image of the $Fe_3O_4$@$MnO_2$ BBHs as shown in Figure 5A, showed that the composite is relative uniform and highly dispersed with a diameter of ~600-800 nm. The size, shape and ball-in-ball hollow spheres of the $Fe_3O_4$@$MnO_2$ were maintained after etching, suggesting the little effect of the etching process to the external hierarchical $MnO_2$ shell and inner $Fe_3O_4$ core (Figure 5B and C). The magnified SEM image (Figure 5D) gave further information about the surfaces of the $Fe_3O_4$@$MnO_2$ BBHs with abundant, randomly assembled thin nanosheets, which would maximize the available active sites for the improvement of catalytic performance. The typical interlayer spacing of 0.25 nm was measured by HRTEM (Figure 5E), corresponding to the (111) planes of $MnO_2$.[45] The EDS of $Fe_3O_4$@$MnO_2$ BBHs showed the presence of Fe, Mn, O and trace amount of C element without Si signal, further corroborating the complete etching of the $SiO_2$ spheres (Figure 5F). The elemental mapping images indicated that Fe and Mn were uniformly dispersed on the inner and outer shell, and this further confirmed successful synthesis of ball-in-ball hollow spheres (Figure 5G). The TEM images of $Fe_3O_4$ solid/hollow spheres (A and B) and hierarchical $MnO_2$ hollow/solid spheres (C and D) were also investigated and the detail was in Figure S1.

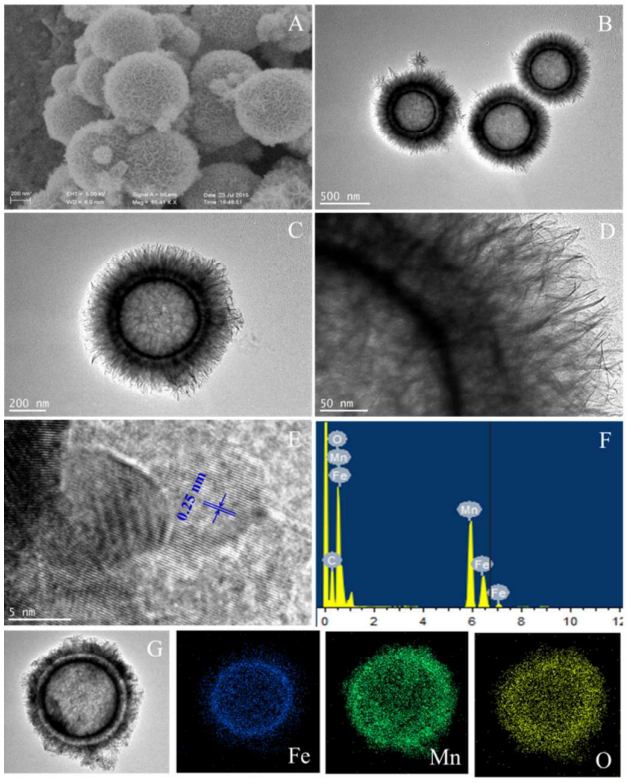


Figure 5. The SEM image (A), TEM images (B, C and D), HRTEM image (E), EDS image (F) and elemental mapping images (G) of $Fe_3O_4$@$MnO_2$ BBHs.

**3.2 Catalytic performances**

The catalytic activities of the synthesized catalysts toward PMS activation were evaluated by MB degradation, as shown in Figure 6A, as well as the comparison with controlled mono-catalytic systems, such as the blank solution, PMS, $Fe_3O_4$ hollow spheres (Hs), $MnO_2$ Hs and $Fe_3O_4$@$MnO_2$ BBHs. Limited degradation efficiencies were observed for the controlled mono-catalytic systems, and trace amounts of MB were degraded in ~90 min. For the bi-catalytic systems by combining the metal catalysts and PMS, the catalytic activity abided by the order of $Fe_3O_4$@$MnO_2$ BBHs > $MnO_2$ Hs > $Fe_3O_4$ Hs+$MnO_2$ Hs > $MnO_2$ solid > $Fe_3O_4$ Hs > $Fe_3O_4$ solid.

Within ~30 min, ~63.7 and ~24.5 % MB were degraded by $MnO_2$ Hs and $Fe_3O_4$ Hs in the presence of PMS, respectively. As expected, a mixture of both $MnO_2$ Hs and $Fe_3O_4$ Hs resulted in a medium catalytic efficiency of ~47.6 % degradation. For comparison, the $Fe_3O_4$ and $MnO_2$ solid spheres with the corresponding values of ~12.6 and ~35.2 % within ~30 min, which were lower than their corresponding hollow spheres due to the hollow structure with more available active sites of the $Fe_3O_4$ and $MnO_2$ Hs. The highest degradation efficiency was detected for the $Fe_3O_4$@$MnO_2$ BBHs with a complete degradation of MB within ~30 min, which was much higher than the combined catalysts of $Fe_3O_4$ Hs + $MnO_2$ Hs, indicating a synergistic catalytic effect of the $Fe_3O_4$@$MnO_2$ BBHs.

The degradation kinetics were fitted with the pseudo-first-order kinetic model, as presented in Figure S2. The calculated

rate constant ($k_{obs}$) were collected in Table S1 with high regression coefficiencies. The highest apparent reaction rate constant was found for the $Fe_3O_4$@$MnO_2$ BBHs with a value of ~1.63 × $10^{-1}$ $min^{-1}$, which was ~74.3, 17.8, 14.2, 8.7 and 5.2 folds higher than that of $Fe_3O_4$ solid spheres, $Fe_3O_4$ Hs, $MnO_2$ solid spheres, $Fe_3O_4$ Hs+$MnO_2$ Hs and $MnO_2$ Hs, respectively.

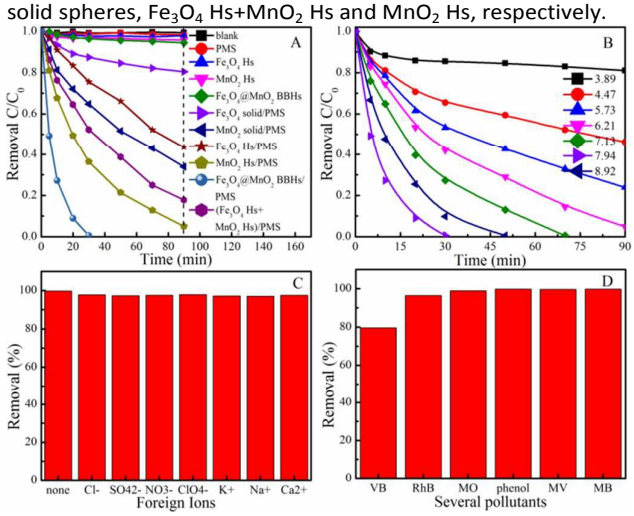


Figure 6. The MB removal in different PMS systems ($C_{catalyst}$= 300 mg/L, $C_0$= 30 mg/L, $C_{PMS}$= 20 mM, pH ~7.94) (A), effect of initial pH (B) and foreign ions (C) on MB degradation by PMS, the catalytic activities of $Fe_3O_4$@$MnO_2$ BBHs for the degradation of various model pollutants (D).

The influence of pH values on MB degradation by the catalyst system of $Fe_3O_4$@$MnO_2$ BBHs/PMS was examined and shown in Figure 6B. The MB degradation efficiency was enhanced as the pH increased from ~3.89 to ~7.94 as observed by the increment of the $k_{obs}$ from ~1.6 × $10^{-3}$ to ~1.63 × $10^{-1}$ $min^{-1}$. A further increase of pH value to ~8.92 resulted in a decreased apparent constant from ~1.63 × $10^{-1}$ to ~1.01 × $10^{-1}$ $min^{-1}$ (Figure S1 and Table S1). This phenomenon can be explain as follows: in weak acidic conditions (pH ~3.89-7.94), the electrostatic interactions between $HSO_5^-$ and the catalyst surface dominated with negligible hydrogen-bondings between $H^+$ and $HSO_5^-$.[47] As the pH increased to ~8.92, the self-decomposition of $HSO_5^-$ initiated, resulting in the decreased degradation efficiency.[18] The highest degradation efficiency at neutral pH made it easier for the practical treatment of the surface and ground water. The pH variation during the reaction in the $Fe_3O_4$@$MnO_2$ BBHs system was also investigated and the detail was in Figure S3.

To mimic the natural wastewater, various foreign ions, including $Cl^-$, $NO_3^-$, $SO_4^{2-}$, $ClO_4^-$, $Na^+$, $K^+$ and $Ca^{2+}$, and other model dyes, such as VB, RhB, MO, phenol and MV, were added into the solution to investigate the catalytic efficiencies of the $Fe_3O_4$@$MnO_2$ BBHs/PMS catalytic system, as shown in Figure 6C and D, respectively. The catalytic efficiency toward MB degradation was not affected by the foreign ions as no obvious decrement of catalytic efficiencies was observed, indicating the high selectivity of $Fe_3O_4$@$MnO_2$ BBHs/PMS catalytic system for MB degradation (Figure 6C). On the contrary, nearly all the tested dyes can be degraded (Figure 6D) with high efficiency, implying a broad application of this catalytic system toward the organic pollutants.

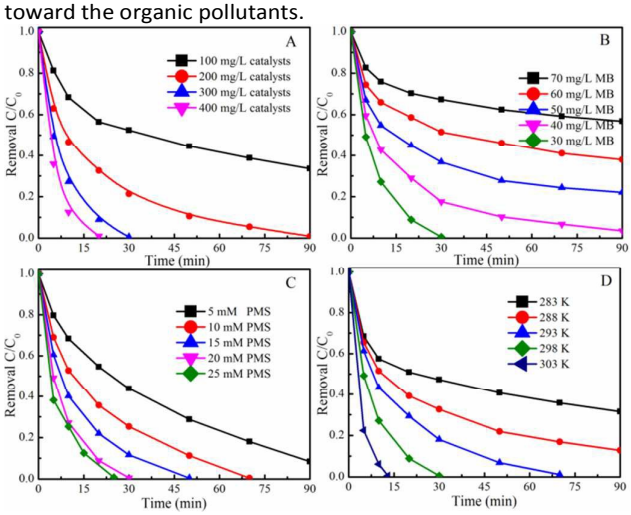


Figure 7. Effects of catalyst loading (A), initial MB concentration (B), PMS concentration (C) and reaction temperature (D) for MB degradation by the $Fe_3O_4$@$MnO_2$ BBHs/PMS catalytic system.

Other influencing factors, including the catalyst loading, MB concentration, PMS dosage and solution temperature, were also evaluated and shown in Figure 7. As expected, higher catalyst loading led to faster MB degradation within shorter contact time. Specifically, the degradation percentages increased from ~66.4% (within ~90 min at 100 mg/L catalyst) to ~99.8% (within ~30 min at 300 mg/L catalyst) and ~99.7% (within ~20 min at 400 mg/L catalyst). Meanwhile, the degradation rate constants ($k_{obs}$) rapidly increased from ~1.08 × $10^{-2}$ to ~2.28 × $10^{-1}$ $min^{-1}$ (Figure S4A and Table S2). This phenomenon was ascribed to the increased active sites with the increasing catalyst loading, resulting in the fast generation of active radicals for MB degradation. On the contrary, decreased degradation efficiencies (~99.8 to ~43.3%) and $k_{obs}$ values (~1.63 × $10^{-1}$ to ~5.15 × $10^{-3}$ $min^{-1}$) were detected with increasing initial MB concentrations from 30 to 70 mg/L (Fig. 7B). This is within expectation because two possible reasons. 1) More reactive sites on the $Fe_3O_4$@$MnO_2$ BBHs surface will be covered by higher concentrations of MB, leading to lower catalytic activities for PMS activation.[21] 2) Higher concentrations of MB required more active radicals for degradation while no extra active radicals can be generated to compensate the increased MB concentrations.[21]

The increased PMS concentrations had the same effect as the catalyst loading increment to accelerate the catalytic efficiencies by generating more active radicals. The time required for complete MB degradation reduced from ~150 to ~20 min as the PMS concentration increased from 5 to 20 mM (Figure 7C), as well the increment of $k_{obs}$ values from ~2.53 × $10^{-2}$ to ~1.63 × $10^{-1}$ $min^{-1}$ (Table 2). The slight decrement of the catalytic efficiency from 20-25 mM was attributed to the self-quenching of $SO_4^{\cdot-}$ by excess PMS.[24]

Moreover, the catalytic activities were dramatically increased at elevated temperatures. For example, ~68.5 and ~87.2% MB

was degraded within ~90 min at 283 and 288 K, respectively, while complete MB degradation was obtained within ~70, ~30, and ~13 min at 293, 298 and 303 K, respectively (Figure 7D). The $k_{obs}$ of MB degradation dramatically increased from ~1.03 × $10^{-2}$ to ~3.67 × $10^{-1}$ $min^{-1}$ as the reaction temperature increased from 283 to 303K (Figure S5A and Table 2). This observation can be explained by the acceleration of active radical generation at elevated temperatures, implying an endothermic degradation process.[21]

The possible reactive species in this degradation system might involve ·OH, $SO_4^{\cdot-}$ and $SO_5^{\cdot-}$. To evaluate the role of these active species, individual scavengers were added to the PMS system. The scavengers used were ethanol for ·OH and $SO_4^{\cdot-}$, TBA for ·OH but not for $SO_4^{\cdot-}$, while $SO_5^{\cdot-}$ could not effectively degrade MB for its lower redox potential.[24, 48] The results of quenching tests for each scavenger were collected in Figure 8A. A dramatic decreased catalytic efficiency was observed from ~99.8% to ~11.8% within ~150 min by the addition of ethanol, indicating that the radicals generated in the system were mostly quenched. The presence of TBA resulted in a slight decreased catalytic efficiency to ~85.9 % within ~55 min, implying the minor contribution of ·OH radicals to MB degradation. Correspondingly, the $k_{obs}$ values decreased from ~1.63 × $10^{-1}$ to ~0.8 × $10^{-3}$ and 6.24 × $10^{-2}$ $min^{-1}$ after the addition of ethanol and TBA (Figure S3B and Table S2). Thus, both $SO_4^{\cdot-}$ and ·OH should be considered as the radical species for MB degradation, of which $SO_4^{\cdot-}$ made dominant contributions.

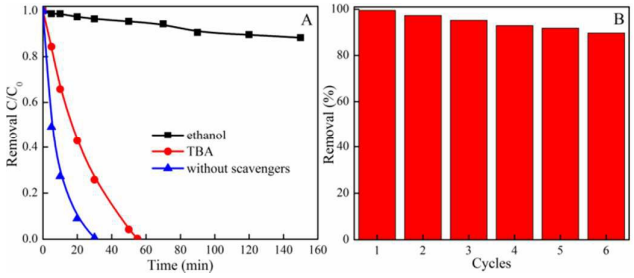


Figure 8. Effect of radical scavengers on MB degradation (A) and MB removal efficiencies within ~30 min at each cycle (B).

The stability and recyclability is a crucial concern with regard to the practical application of the catalyst, as shown in Figure 8B. It was found that the catalytic efficiencies were only slight decreased even after six successive cycles with a removal efficiency still higher than ~90%. To further investigate the stability, ICP-MS measurements were performed to detect the possible Fe and Mn leaching after the catalytic reaction. The percentage of Fe and Mn leaching in a $Fe_3O_4$@$MnO_2$ BBHs-PMS system changed gently at a lower level of 0.22-0.45% and 0.51-0.87% within reaction time, respectively. This finding verified the excellent stability of the $Fe_3O_4$@$MnO_2$ BBHs. Moreover, the XRD pattern and TEM image of the recovered catalyst revealed that the $Fe_3O_4$@$MnO_2$ BBHs crystalline and structures was scarcely changed (Figure S6), indicating the excellent stability, high reusability and prominent catalytic activity of the as-prepared $Fe_3O_4$@$MnO_2$ BBHs/PMS system. Further, the mineralization degree of MB in $Fe_3O_4$@$MnO_2$ BBHs-PMS system was evaluated through the degree of TOC removal. In fact, the total mineralization of an organic compound such as MB containing C, S, and N functions leads generally to the formation of $CO_2$, $SO_4^{2-}$, $NH_4^+$ and/or $NO_3^-$. As seen in Figure S7, ~55% of TOC removal was reached within ~30 min. The residual TOC may associate with some small molecular organic acids generated from the catalytic reaction.

Based on the above discussion, a plausible catalytic mechanism was proposed and different layers of the catalyst exhibited different functions during the degradation process. A schematic illustration was depicted in Figure 9 by dividing the catalytic system into three sections.

The outside layer was filled with hierarchical $MnO_2$ nanosheets, which could catalyze the generation of active radicals from PMS and accumulate MB from the bulk solutions to initiate degradation. The reactions were proposed as follows: [2, 28]

≡Mn(IV)+$HSO_5^-$→≡Mn(III) + $SO_4^{\cdot-}$ + $OH^-$

≡Mn(IV)+$HSO_5^-$→≡Mn(III) + $SO_4^{2-}$ + ·OH

≡Mn(III)+$HSO_5^-$→≡Mn(IV) + $SO_5^{\cdot-}$ + $H^+$

$SO_4^{\cdot-}$ + $H_2O$→$SO_4^{2-}$ + ·OH + $H^+$

$SO_4^{\cdot-}$ + ·OH + MB→ degradation products

The second layer of the catalytic system was comprised of the inner $MnO_2$ layers of the shell together with the outer surfaces of $Fe_3O_4$ balls. Both $MnO_2$ and $Fe_3O_4$ would react with PMS to generate active radicals, resulting accelerated degradation rate. The corresponding degradation reactions were listed below:[4, 12, 18, 19]

≡Mn(IV)+$HSO_5^-$→≡Mn(III) + $SO_4^{\cdot-}$ + $OH^-$

≡Mn(III)+$HSO_5^-$→≡Mn(IV) + $SO_5^{\cdot-}$ + $H^+$

≡Fe(II)+$HSO_5^-$→≡Fe(III)+ $SO_4^{2-}$ + ·OH

≡Fe(II)+$HSO_5^-$→≡Fe(III)+ $SO_4^{\cdot-}$+ $OH^-$

≡Mn(III) + Fe(III) →≡Mn(IV) + ≡Fe(II)

$SO_4^{\cdot-}$ + $H_2O$→$SO_4^{2-}$ + ·OH + $H^+$

$SO_4^{\cdot-}$ + ·OH + MB→ degradation products

The inner surface of the $Fe_3O_4$ balls also had a large number of active sites, which could also be beneficial for the heterogeneous degradation reaction. This is the third layer of the reaction area with the proposed reaction equations.[19]

≡Fe(II)+$HSO_5^-$→≡Fe(III)+ $SO_4^{2-}$ + ·OH

≡Fe(II)+$HSO_5^-$→≡Fe(III)+ $SO_4^{\cdot-}$+ $OH^-$

$SO_4^{\cdot-}$ + $H_2O$→$SO_4^{2-}$ + ·OH + $H^+$

$SO_4^{\cdot-}$ + ·OH + MB→ degradation products

As for the cavity of the ball-in-ball hollows, the accumulated MB will be confined within these microenvironments, leading to higher instantaneous MB concentrations in the interior of the nanoreactor and thus affording a driving force to increase the degradation rate.

To evaluate the effect of natural dissolved matter in an artificial system, the performance of the present method for real water sample analysis was challenged by lake water samples obtained from the Daming Lake of Jinan, Shandong province, China. The lake water samples were filtered through a 0.22 μm membrane and then centrifuged at 10000 rpm for 40 min. The resultant water samples were spiked with MB (30 mg/L) and then analyzed with the proposed method. Within ~30 min, ~83.5% MB was degraded by $Fe_3O_4$@$MnO_2$ BBHs in the presence of PMS. The high degradation efficiency at real

water sample made it easier for the practical treatment of the surface and ground water.

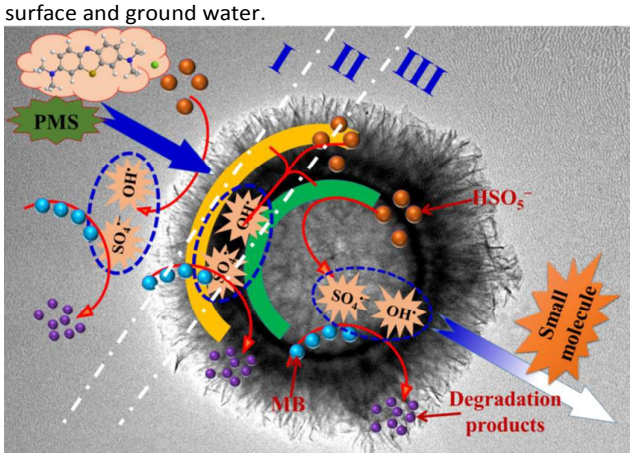


Figure 9. The proposed mechanism of the PMS activation by $Fe_3O_4$@$MnO_2$ BBHs for MB degradation.

## Conclusions

In summary, novel ball-in-ball hollow structural nanocomposites, $Fe_3O_4$@$MnO_2$ BBHs, were fabricated with $Fe_3O_4$ hollow cores and hierarchical $MnO_2$ shells for the first time through a facile and simple strategy, which were subjected to MB degradation with the aid of PMS as the active radical sources, exhibiting the highest catalytic activity and stability as compared with other catalysts, such as $MnO_2$ Hs, $Fe_3O_4$ Hs and a combination of both. This enhanced catalytic activity can be explained by the synergistic effect of outer $MnO_2$ nanosheets and inner $Fe_3O_4$ hollow ball. The inherent magnetic property of the as-prepared catalyst made it easier for recyclability, and slightly decreased catalytic efficiency was observed after six consecutive recycles. The degradation mechanism was also investigated by examining the contributions of different active radicals, followed by the proposal of a plausible degradation mechanism. This work provided new strategies for the controllable synthesis of complex hollow structures with multi-component functional nanomaterials in the application of environmental issues.

## Acknowledgements

Financial supports from NSFC (Grant No. 21272236, 11304120 and 21225730), the Chinese National Fusion Project for ITER (2013GB110005) and the special scientific research fund of public welfare profession (environmental protection) of China (201509074).

## Notes and references

1 J. Ma, F. Yu, L. Zhou, L. Jin, M. X. Yang, J. S. Luan, Y. H. Tang, H. B. Fan, Z. W. Yuan and J. H. Chen, *ACS Appl. Mater. Interfaces*, 2012, **4**, 5749-5760.
2 E. Saputra, S. Muhammad, H. Sun, H.-M. Ang, M. O. Tadé and S. Wang, *Appl. Catal. B: Environ.*, 2013, **142-143**, 729-735.
3 X. L. Yang, X. Y. Wang, Y. Q. Feng, G. Q. Zhang, T. S. Wang, W. G. Song, C. Y. Shu, L. Jiang and C. R. Wang, *J. Mater. Chem. A,* 2013, **1**, 473-477.
4 X. L. Yu, S. R. Tong, M. F. Ge, J. C. Zuo, C. Y. Cao and W. G. Song, *J. Mater. Chem. A,* 2013, **1**, 959-965.
5 Y. X. Zhang, X. Y. Yu, Z. Jin, Y. Jia, W. H. Xu, T. Luo, B. J. Zhu, J. H. Liu and X. J. Huang, *J. Mater. Chem.,* 2011, **21**, 16550-16557.
6 J. Qu, L. Shi, C. He, F. Gao, B. Li, Q. Zhou, H. Hu, G. Shao, X. Wang and J. Qiu, *Carbon*, 2014, **66**, 485-492.
7 Y. Shao, L. Zhou, C. Bao and J. Ma, *Carbon*, 2015, **89**, 378-391.
8 R. Huang, Y. Liu, Z. Chen, D. Pan, Z. Li, M. Wu, C. H. Shek, C. M. Wu and J. K. Lai, *ACS Appl. Mater. Interfaces*, 2015, **7**, 3949-3959.
9 K.-T. Lee, X.-F. Chuah, Y.-C. Cheng and S.-Y. Lu, *J. Mater. Chem. A*, 2015, **3**, 18578-18585.
10 Y. Su, Z. Wu, Y. Wu, J. Yu, L. Sun and C. Lin, *J. Mater. Chem. A*, 2015, **3**, 8537-8544.
11 J. Fan, X. Jiang, H. Min, D. Li, X. Ran, L. Zou, Y. Sun, W. Li, J. Yang and W. Teng, *J. Mater. Chem. A*, 2014, **2**, 10654-10661.
12 D. Chen, X. Ma, J. Zhou, X. Chen and G. Qian, *J. Hazard. Mater.*, 2014, **279**, 476-484.
13 Y. Liu, Z. Chen, C. H. Shek, C. M. Wu and J. K. Lai, *ACS Appl. Mater. Interfaces*, 2014, **6**, 9776-9784.
14 Y. Li, J. Qu, F. Gao, S. Lv, L. Shi, C. He and J. Sun, *Appl. Catal. B: Environ.*, 2015, **162**, 268-274.
15 Y. Wang, H. Sun, H. M. Ang, M. O. Tade and S. Wang, *ACS Appl. Mater. Interfaces*, 2014, **6**, 19914-19923.
16 T. Zhang, H. Zhu and J. P. Croue, *Environ. Sci. Technol.*, 2013, **47**, 2784-2791.
17 Y. Wang, H. Sun, X. Duan, H. M. Ang, M. O. Tadé and S. Wang, *Appl. Catal. B: Environ.*, 2015, **172-173**, 73-81.
18 M. Feng, R. Qu, X. Zhang, P. Sun, Y. Sui, L. Wang and Z. Wang, *Water Res.*, 2015, **85**, 1-10.
19 C. Tan, N. Gao, Y. Deng, J. Deng, S. Zhou, J. Li and X. Xin, *J. Hazard. Mater.*, 2014, **276**, 452-460.
20 W.-D. Oh, Z. Dong, Z.-T. Hu and T.-T. Lim, *J. Mater. Chem. A*, 2015, DOI: 10.1039/c5ta06563a.
21 X. Duan, K. O'Donnell, H. Sun, Y. Wang and S. Wang, *Small*, 2015, **11**, 3036-3044.
22 Y. Yao, Y. Cai, G. Wu, F. Wei, X. Li, H. Chen and S. Wang, *J. Hazard. Mater.*, 2015, **296**, 128-137.
23 K.-Y. A. Lin, F.-K. Hsu and W.-D. Lee, *J. Mater. Chem. A*, 2015, **3**, 9480-9490.
24 T. Zeng, X. Zhang, S. Wang, H. Niu and Y. Cai, *Environ. Sci. Technol.*, 2015, **49**, 2350-2357.
25 E. Saputra, S. Muhammad, H. Sun, H. M. Ang, M. O. Tade and S. Wang, *Environ. Sci. Technol.*, 2013, **47**, 5882-5887.
26 X. Duan, Z. Ao, H. Sun, S. Indrawirawan, Y. Wang, J. Kang, F. Liang, Z. Zhu and S. Wang, *ACS Appl. Mater. Interfaces*, 2015, **7**, 4169-4178.
27 W.-D. Oh, S.-K. Lua, Z. Dong and T.-T. Lim, *J. Mater. Chem. A*, 2014, **2**, 15836-15845.
28 Y. Wang, H. Sun, H. M. Ang, M. O. Tadé and S. Wang, *Appl. Catal. B: Environ.*, 2015, **164**, 159-167.
29 J. Liu, Z. Zhao, P. Shao and F. Cui, *Chem. Eng. J.*, 2015, **262**, 854-861.
30 T. Zeng, X. Zhang, S. Wang, Y. Ma, H. Niu and Y. Cai, *Chem.-Eur. J.*, 2014, **20**, 6474-6481.
31 J. Bai, X. Li, G. Liu, Y. Qian and S. Xiong, *Adv. Funct. Mater.*, 2014, **24**, 3012-3020.
32 F. Wu, S. Xiong, Y. Qian and S. H. Yu, *Angew. Chem. Int. Edit.*, 2015, **54**, 10787-10791.
33 F. Wu, C. Yu, W. Liu, T. Wang, J. Feng and S. Xiong, *J. Mater. Chem. A*, 2015, **3**, 16728-16736.
34 G. Zhang, L. Yu, H. B. Wu, H. E. Hoster and X. W. D. Lou, *Adv. Mater.*, 2012, **24**, 4609-4613.

35 L. Shen, L. Yu, H. B. Wu, X.-Y. Yu, X. Zhang and X. W. D. Lou, *Nat. Comm.*, 2015, **6**.
36 X. Y. Yu, L. Yu, L. Shen, X. Song, H. Chen and X. W. D. Lou, *Adv. Funct. Mater.*, 2014, **24**, 7440-7446.
37 G. Zhang and X. W. D. Lou, *Angew. Chem. Int. Edit.*, 2014, **126**, 9187-9190.
38 J. Wang, N. Yang, H. Tang, Z. Dong, Q. Jin, M. Yang, D. Kisailus, H. Zhao, Z. Tang and D. Wang, *Angew. Chem. Int. Edit.*, 2013, **125**, 6545-6548.
39 P. Xu, R. Yu, H. Ren, L. Zong, J. Chen and X. Xing, *Chem. Sci.*, 2014, **5**, 4221-4226.
40 J. Qi, K. Zhao, G. Li, Y. Gao, H. Zhao, R. Yu and Z. Tang, *Nanoscale*, 2014, **6**, 4072-4077.
41 Z. Dong, H. Ren, C. M. Hessel, J. Wang, R. Yu, Q. Jin, M. Yang, Z. Hu, Y. Chen and Z. Tang, *Adv. Mater.*, 2014, **26**, 905-909.
42 T. Zeng, X. Zhang, Y. Ma, S. Wang, H. Niu and Y. Cai, *Chem. Commun.*, 2013, **49**, 6039-6041.
43 T. Zeng, X. Zhang, S. Wang, Y. Ma, H. Niu and Y. Cai, *J. Mater. Chem. A*, 2013, **1**, 11641-11647.
44 X. Tang, Z.-h. Liu, C. Zhang, Z. Yang and Z. Wang, *J. Power Sources*, 2009, **193**, 939-943.
45 L. Li, R. Li, S. Gai, S. Ding, F. He, M. Zhang and P. Yang, *Chem.-Eur. J.*, 2015, **21**, 7119-7126.
46 T. Pal, R. Sahoo, M. Pradhan, A. Roy, S. Dutta, C. Ray, Y. Negishi and A. Pal, *Chem. Asian J.*, 2015.
47 Y. Lei, C. S. Chen, Y. J. Tu, Y. H. Huang and H. Zhang, *Environ. Sci. Technol.*, 2015, **49**, 6838-6845.
48 Y.-P. Zhu, T.-Z. Ren and Z.-Y. Yuan, *Nanoscale*, 2014, **6**, 11395-11402.

## Graphical Abstract

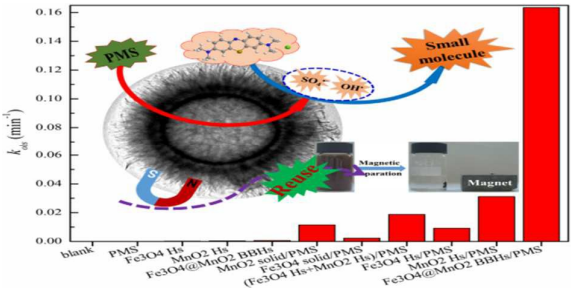


$Fe_3O_4$@$MnO_2$ ball-in-ball hollow spheres are fabricated through a facile and simple strategy, exhibiting the excellent catalytic activity and stability.